Coupled morphological and structural evolution of δ-MnO2 to α-MnO2 through multistage oriented assembly processes: the role of Mn(III)

Xinran Liang, Jeffrey E Post, Bruno Lanson, Xiaoming Wang, Mengqiang Zhu, Fan Liu, Wenfeng Tan, Xionghan Feng, Guomin Zhu, Xin Zhang, et al.

Coupled Morphological and Structural Evolution of δ-MnO_2 to α-MnO_2 through multistage Oriented Assembly processes: the role of Mn(III)

Xinran Liang,[†] Jeffrey E. Post,[‡] Bruno Lanson,[§] Xiaoming Wang,[†] Mengqiang Zhu,[⊥] Fan Liu,[†] Wenfeng Tan,[†] Xionghan Feng,[†*] Guomin Zhu, Xin Zhang and James. J. De Yoreo

[†] *Key Laboratory of Arable Land Conservation (Middle and Lower Reaches of Yangtse River), Ministry of Agriculture, College of Resources and Environment, Huazhong Agricultural University, Wuhan 430070, China*

[‡] *Department of Mineral Sciences, Smithsonian Institution, Washington, DC 20013, USA*

[§] *University of Grenoble Alpes, CNRS, ISTerre, F-38000 Grenoble, France*

[⊥] *Department of Ecosystem Science and Management, University of Wyoming, Laramie, WY, 82071, United States.*

Physical Sciences Division, Pacific Northwest National Laboratory, Richland, WA99352, USA

KEYWORDS: δ-MnO_2; α-MnO_2; morphology evolution; structure transformation; Mn(III).

ABSTRACT: The efficient assembly of nanoparticles by oriented attachment (OA) mechanism has attracted more and more attention. However, the morphological and structural coupling during the OA processes is not fully understood. Here, we propose the OA mechanism during the layer-based δ-MnO_2 transformation to tunnel-based α-MnO_2 using powder X-ray diffraction, X-ray atomic pair distribution function and transmission electron microscopy. It is suggested staged three-dimensional OA processes play a vital role in both morphological and concurrent structural evolution of δ-MnO_2 into α-MnO_2. In the initial stage of the evolution, the δ-MnO_2 nanodots are found to spontaneously self-assemble into long nanosheet via OA process along a-b plane driven by hydrogen bonding through edge sites. Meanwhile, the Mn(IV) in the [MnO_6] octahedral layers are reduced to Mn(III)/Mn(II) by H_2O with the release of O_2 and oxygen vacancies generation in the δ-MnO_2 structure. The newly formed Mn(III) which migrates from layers to above/below the vacancies coordinate with three hydroxide oxygen. Therefore, the adjacent long nanosheets attach with each other driven by hydrogen bonding between hydroxide oxygen which coordinated with interlayer Mn(III) and form primary nanorods through face-to-face OA mechanism along *c*-axis. Concomitantly, the bonding of [Mn(III)O_6] octahedra in interlayer of long nanosheets with adjacent [MnO_6] octahedral layers were facilitated to construct the new 2×2 tunnel α-MnO_2. These findings provide insight not only on mechanism of transformation of layer-based nanoparticles to tunnel-based nanoparticles but also on the efficient controlled synthesis and design of nanomaterials through different structures and morphologies.

Nonclassical mechanism of crystal growth, oriented attachment (OA), proceeds by repeated attachment events of crystalline particles on specific crystal faces that are lattice-matched with true crystallographic alignment.[1] The growth of many crystalline substances, including both engineered nanomaterials and naturally-occurring nanoparticles, has been reported via OA mechanism.[2] As OA is a process of efficient assembly of primary particle units, such bottom-up fabrication can produce the novel materials with the versatile properties. These properties of nanoparticles closely related to not only morphology but also structure. The OA process only leads to morphology evolution by previous reported, while the processes of structure changes associated with morphology evolutions were less explored. Revealing the coupling relationship between morphology evolutions and structure changes during the OA process is not only important for controlling the synthetic materials but also proving a novel idea for the study of crystal growth.[3]

Recently, more and more studies reported that poor crystalline layer manganese oxides (LMOs) nanoparticles assemble to LMOs nanoflower and tunneled manganese oxides (TMOs) nanorod by OA mechanism.[4-8] And the LMOs and TMOs are widely applied as materials in catalysis, ion exchange, energy storage and octahedral molecular sieves.[9-10] In addition, LMOs-to-TMOs reaction mechanisms have been widely investigated because LMOs association with TMOs occur frequently in the environment.[5, 8-10] There are some detailed studies about the structure evolution and limited studies about the morphology evolution during LMOs-to-TMOs reaction, respectively.[8, 11]The two separate studies on the structure and morphology evolution bring some difficulties in full understanding of the LMOs-to-TMOs reaction mechanism.

α-MnO_2 represents an important family of TMOs with 2×2 and 1×1 tunnel structure which formed by double chains of edge-sharing [MnO_6] octahedra share corners with neighboring chains.[12] The larger 2×2 tunnels are generally stabilized by K^+, Ba^+ and Na^+.[13] The unique physicochemical properties of α-MnO_2 have given this material a wide range of potential applications in gas sensing, catalysis, energy storage, separation (molecular sieves), and battery materials.[14-16] These properties are greatly

affected by the structure and morphology of α-MnO_2.[16]

The δ-MnO_2, as an important LMO, is associated with the α-MnO_2 frequently in the environmental.[11] It was proposed that formation and migration of Mn(III) occurred during structural transformation of δ-MnO_2 into α-MnO_2.[17] And a detailed OA process by which α-MnO_2 long nanorods form from α-MnO_2 primary nanorods was also reported.[16, 18] However, the formation process of α-MnO_2 primary nanorods from poorly-crystalline δ-MnO_2 nanodots is not understood.[19] In addition, it is unclear how the new tunnel structure formation corresponds with morphology evolution by the OA process. A basic knowledge of the morphology evolution across the whole synthesis process and the relationship with structural transformation are also critical for the α-MnO_2 material synthesis in application and understanding of the minerology and behavior of δ-MnO_2 and α-MnO_2 type minerals in the nature.

In this study, Na^+/K^+-stabilized α-MnO_2 nanorods were synthesized by co-precipitation of Na/$KMnO_4$ with $MnSO_4$.The dynamic process of Na^+-stabilized α-MnO_2 nanorods formation is carefully explored; because the Na phase forms at a slower rate than that of K^+-stabilized, as shown in previous experiments.[13], it provides a more suitable system for study. During the synthesis, intermediate products were sampled and quenched in liquid N_2 at different time intervals to stop crystal growth and capture in-situ morphologies and structures. These intermediate products were examined by powder X-ray diffraction (XRD), pair distribution function (PDF), and X-ray photoelectron spectroscopy (XPS) to investigate the structure changes at the atomic level. Meanwhile, morphological changes during the formation process were revealed by using high-resolution transmission electron microscopy (HRTEM) and field-emission scanning electron microscopy (FESEM). Possible explanations for the observed relationship between morphologic and structural evolutions are proposed.

RESULTS AND DISCUSSION

$$2MnO_4^- + 3Mn^{2+} + 2H_2O \rightarrow 5\delta\text{-}MnO_2 + 4H^+ \qquad (1)$$

During the synthesis of δ-MnO_2, the amount of MnO_4^- was in excess compared to the Mn(II) shown in equation 1. Therefore, the supernatant was purple after the two

solutions were mixed. After the solution was heated to 100 C for 14 min, the color of the supernatant changed from purple to colorless due to the complete reduction of MnO_4^- ions under the acidic condition (pH=0.86):[18, 20], according to equation 2.

$$4MnO_4^- + 4H^+ \rightarrow 4\delta\text{-}MnO_2 + 3O_2 + 2H_2O \quad (2)$$

The reaction rate for formation of δ-MnO_2 by equ. 2 is much slower than that of equ. 1.[18] The structures and the morphologies ofδ-MnO_2 from these two pathways were characterized by XRD and HRTEM, Figure 1 and 3, and appear to be identical.

Structural evolution. The powder XRD pattern of the initial δ-MnO_2 shows two broad diffraction peaks at 37° ($d_{(100)}$ = 2.46 Å) and 65° ($d_{(110)}$ = 1.43 Å) (Figure 1A), which can be attributed to δ-MnO_2 with poorly-crystalline, small sized, randomly stacked [MnO_6] octahedral layers.[7, 18, 21] The *d*-spacing ratio of $d_{(100)}$ to $d_{(110)}$ is 1.73, indicating a hexagonal layer symmetry.[22-24] The absence of basal (001) and (002) peaks ($d_{(001)}$ = 7.2 Å , $d_{(002)}$ = 3.6 Å) is indicative of stacking of only a few [MnO_6] octahedral layers along the *c*-axis.[22, 25-26]

Before the suspension was heated at 100 ℃ for 10 min, only δ-MnO_2 appeared in the XRD pattern (Figure 1A, B). The (100) and (110) diffraction peaks of δ-MnO_2 are not sharper than those for the initially formed sample, indicating that the sizes of the crystallites did not increase within the a-b planes (Figure 1B), which is consistent with previous reports.[17] A detailed inspection of these (100) and (110) peaks in Figure. 1B suggests a slight structural alteration of the δ-MnO_2, evidenced by the appearance of a small shoulder on the high angle side of the (100) peak., Previous studies proposed that this feature could be related to an increased amount of Mn(III) capped on vacancies in the [MnO_6] octahedral layers.[21] These results suggest that Mn(IV) is being reduced to Mn(III)/Mn(II) and adsorbed on the vacancy sites with increasing heating time.

After the suspension was heated for 14 min, weak (110), (200) and (310) peaks of α-MnO_2 (ICDD No. 00-29-1020, $d_{(110)}$ = 0.69nm, $d_{(200)}$ = 0.48nm and $d_{(310)}$ = 0.31 nm) appeared, indicating that some of the δ-MnO_2 was transforming to α-MnO_2 between heating from 10 min to 14 min (Figure 1A).[16] The peak widths narrowed and their intensities increased gradually during heating from 14 to 20 min, indicating that crystallite size and crystallinity of α-MnO_2 increased.. The evolution of the α-MnO_2

crystal morphology with structure transformation is explored below.

From a peak intensity examination of the pair distribution functions (PDF), a systematic structural change is observed during the synthesis process (Figure 2A). From Na100-6 to Na80, peaks at 2.85 Å and 4.93 Å decrease in intensity.[27] These peaks are attributed to atomic pairs involving t first and second Mn shells within the octahedral layer around a given Mn (Mn_L-Mn_L1 and Mn_L-Mn_L2 shells).[21, 27] Contrastingly, correlations at 3.44 Å and 5.28 Å increase in intensity. They are attributed to pairs formed by a Mn_L and an interlayer Mn (Mn_{IL}) at vacancies belonging respectively to the first (Mn-$Mn_{IL}1$) and second (Mn-$Mn_{IL}2$) shells. The PDF results suggest that Mn_L migrate from the layers to the interlayer, above and below the vacancies, to form mono-μ-oxo bridge (Mn_L-Mn_{IL1} distance of about 3.44 Å) [MnO_6] octahedra.[28] As is discussed below, a possible mechanism for this reaction is the reduction of Mn^{4+} by H^+. It is likely that these interlayer Mn(III)/Mn(II) octahedra act as templates for the tunnel 'walls' during transformation to α-MnO_2.[11-12]

Chemical properties. The Mn average oxidation states (AOS) of the intermediate products provide additional evidence for the Mn(III)/Mn(II) production and structural changes of the δ-MnO_2. The detailed Mn(IV), Mn(III), and Mn(II) contents which are obtained through fitting the XPS narrow scans of the Mn ($2p_{3/2}$) spectra are listed in Table 1. The AOS of the samples decrease from 3.96 to 3.70 (Table 2) before the suspension was heated at 100 ℃ for 10 min. The percentages of Mn(IV) decreased from 83.5 % to 80.5 %, and the percentage of Mn(III) decreased from 14.3 % to 12.3 % and then increased to 15.3% during this stage, indicating that the Mn(IV) and Mn(III) were initially reduced to Mn(II), followed by the comproportionating between vacancy-adsorbed Mn(II) and structural Mn(IV) to form Mn(III). The values of AOS obtained by fitting of XPS spectra are systematically lower than that obtained by titration method probably due to higher content of lower valence Mn present at the surface compared to that in bulk.[29-30] Thus, the XPS-derived AOS represents "surface" Mn AOS, and it is possible that Mn(IV) is reduced to Mn(III)/Mn(II) and adsorbed on the surface of δ-MnO_2 nanoparticles.[29-30] Despite the discrepancy between the absolute AOS values, we see similar trends in the two methods.

Previous studies have shown that structural Mn(III) was critical to the transformation of layer structured Mn oxides into tunneled ones.[11, 31] But the mechanism by which Mn(III) is reduced from Mn(IV) in the initial t δ-MnO_2 is still an open question. As described above, some of the octahedral Mn(IV) was initially reduced to Mn(II), and a portion of that was subsequently transformed to Mn(III). Given that apart from H_2O (H^+) no other reductant exists during the transformation of δ-MnO_2 to α-MnO_2, there are two possible pathways to the reduction of Mn(IV).

One way is that the MnO_2 is reduced by H^+ at ~ 100 ℃ and pH < 1, following the reaction:[32]

$$2MnO_2+4H^++e^-\rightarrow 2Mn^{2+}+2H_2O+O_2 \qquad (3)$$

Depending on solution pH, the Mn(II) cations originating from this partial δ-MnO_2 dissolution might attach above/below layer vacancies.[11] The XRD pattern of NaMix in Figure. 1A shows that the crystallinity of δ-MnO_2 was poor (i.e. crystallite size was small), indicating large surface area, which favors equ. 3. As discussed below, however, HRTEM images suggest that the crystallite sizes increased slightly during heating for 10 min. As the crystallinity of the sample increases, the Mn(IV) dissolution rate slows down, consistent with the rate of the decrease of the AOS of reaching a minimum when the suspension was heated at 100 ℃ for 10 min.

A second possible pathway for reduction of the Mn^{4+}, is for the poorly-crystalline δ-MnO_2, with mixed-Mn valences (II, III and IV) to release structural oxygen, following the reaction:[33]

$$[\text{-Mn(IV)-}O^{2-}\text{-Mn(IV)-}]\rightarrow[\text{-Mn(III)- -Mn(III)-}]+\frac{1}{2}O_2 \qquad (4)$$

The XPS fitting results of O1s are listed in Table. 1. There are three species of oxygen existing in Mn oxides including lattice oxygen (O^{2-}), hydroxide oxygen (-OH), and oxygen in molecular water. Among the three species of oxides, the O^{2-} decreased from 69.9 % to 56.2 %, and the -OH increased from 18.1 % to 26.3 % during the heating of the suspension for the first 10 min. It lost three O^{2-} and produced six -OH When one Mn(III) migrates from [MnO_6] layer to the interlayer, above or below the resulting vacancy, the Mn(III) will be coordinated to three layer O atoms and three OH; the O

atoms on the opposite side of the vacancy, where there is no Mn(III), will complete their charge balance by forming OH. . Although this scenario is consistent with the observed change in XPS values for O^{2-} and OH^-, the decrease in the XPS value for O^{2-} is greater relative to that of OH^- than would be predicted. It is interesting that this great loss of O^{2-} is consistent with creation of O vacancies in the δ-MnO_2, as proposed above (equation 4). Also, some studies have suggested that the observed increase of the O1s XPS peak at 532.4 eV in our XPS spectra is induced by the formation of oxygen vacancies (Figure S3).[34-38] The uncertainties in the XPS values and other structural unknowns, however, make it impossible to draw definite conclusions. It was reported that longer bond of Mn-O, adsorbed ions, and poorly-crystallinity favored the formation of the oxygen vacancies.[33, 39-40] Here, the increase in the content of Na^+ cations and Mn(III) (Table1, 2), and the weakening of the crystallinity could facilitate formation of the oxygen vacancies, which promote Mn(III) production and the transformation of 2D layer structure into 1D tunnel structure.

Interestingly, the intensity of O1s XPS peaks at 532.4 eV reached a maximum and AOS of δ-MnO_2 reached a minimum at heating for 10 min. The reactions described in equ. 3 and equ. 4 became less favorable due to the formation of more stable structure of α-MnO_2 and the percentages of Mn(III) and Mn(II) decreased gradually (Table 1). And the decrease of the O1s XPS peak at 532.4 eV is induced by the reduction of oxygen vacancies (Figure S3). This indicated that dissolved oxygen generated by the previous reactions (equ. 3, 4) could refill into oxygen vacancies and oxidizes Mn(III)/Mn(II) back to Mn(IV), causing increase of AOS from 3.70 to 3.96 (Table 2). Contrarily, the content of -OH and Na^+ reached a maximum when δ-MnO_2 started to transform into α-MnO_2, then decreased during the formation of α-MnO_2. Na^+ cations adsorbed on δ-MnO_2 were released because the adsorption affinity and compensation charge (Mn AOS is close to 4.00) of α-MnO_2 are less than that of δ-MnO_2.[41] In addition, bonding of interlayer Mn(III) to construct tunnel structure resulted in decreased of -OH content and increase O^{2-} content during the suspension was heated at 100 ℃ for 10 min to 20 min. The above analysis further reveals the changes of structures and properties of the intermediates during the transformation process.

Morphology Evolution. High-resolution transmission electron microscopy (HRTEM), field-emission scanning electron microscopy (FESEM) and electron diffraction were used to elucidate the kinetics of the morphological evolution during the phase transformation. Immediately after $NaMnO_4$ and $MnSO_4$ were mixed, a three-dimensional morphology of aggregation of about 100 nm in diameter was observed (Figure 3A), and primary nanodots were observed using HRTEM after ultrasonic dispersion (Figure 3B, C). This indicates that the primary nanodots loosely aggregate, likely driven primarily by surface energy. The edges of the primary nanodots in Figure 3D range from 2 to 4 nm, in good agreement with the coherent scattering domain (CSD) size of 3.2 nm obtained from the PDF data (Figure 2A). The nanodots exhibited d_{hkl} spacing of 0.24 nm, corresponding to the (100) δ-MnO_2 plane, which is consistent with the $d_{(100)}$ = 2.46 Å in XRD patterns (Figure 1A and 3D). Additionally, the absence of (001) and (002) reflections in the XRD patterns indicate that at this stage the poorly crystalline nanodots consists of no more than a few [MnO_6] octahedral layers.

When the suspension is heated for 6 min, long nanosheets appear with lengths ranging from 20 to 60 nm and diameters from 3 to 7 nm (Figure 4A-C). The observed lattice fringes again exhibit a spacing of 0.24 nm, which corresponds to the (100) lattice of δ-MnO_2 (Figure 4B), and are consistent with the SAED pattern in Figure 4D for the area highlighted by the blue square in Figure 4A. An additional diffraction ring at ~0.14 nm, originating from the (110) reflection of δ-MnO_2, is also observed in the SAED pattern (Figure 4D).

The HRTEM observations suggest that the long nanosheets and nanodots are both δ-MnO_2 with different morphologies. The serrated end of the long nanosheets (Figure 4B) and the overall patchwork textures indicate that long nanosheets apparently are formed by direct self-assembly of nanodots. The red circle in Figure 4C indicates a dislocation at the end of long nanosheet, which possibly marks the junction of poorly-crystalline nanodots. The assembly of δ-MnO_2 at low pH is energetically favored because the primary nanodots have high surface energy, low Na^+ content and hydroxyls on edge sites which can generate hydrogen bonding with adjacent nanodots.[4]

Changes in both structure and morphology indicated the conversion of δ-MnO_2

to α-MnO_2 after the suspension was heated for 10 min. The widths and lengths of the long nanosheets increase to ~10-30 nm and ~30-100 nm, respectively (Figure 5A). HRTEM images of cutting the nanosheets along the (001) plane in Figure 5B reveals that long nanosheets are thickened by assembly, and form nanorods ~7 nm thick (The cutting schematic along the (001) plane is shown in Figure S8A). The measured d_{hkl} spacing of 0.69 nm corresponds to the (110) plane of α-MnO_2. The observed nanorods exhibit different sizes and crystallographic orientations due to the assembly of multiple primary nanorods (Figure 5B). Cutting the long nanosheets along the (110) plane (Figure 5C- The cutting schematic along (001) is shown in Figure S8B) shows that the length of long nanosheets is ~ 40 nm. However, the observed thickness of the long nanosheets (2.24 nm) corresponds to only three [MnO_6] octahedral layers. The new [MnO_6] octahedral layer assembled onto the nanosheet has a spacing of 1.29 nm which is larger than the $d_{(110)}$ below (Figure 5C). And the size of this layer in blue square in Figure 5C (6.7 nm) which corresponds to the size of nanodots, which indicating the long nanosheets thicken by face-to-face assembling of nanodots. The blue circle in Figure 5C reveals the dislocation along [001] direction indicate that there are two small nanorods assembled by end-to-end along (001), which is thermodynamically favored because the larger surface energy of (001) plane than that of (110) plane. HRTEM shows that the nanorods with serrated sides form by assembly of long nanosheets (Figure 5D). The IFFT image in Figure 5D shows that there are many lattice dislocations along the α-MnO_2 (110) plane, indicating formation of the long nanosheet by assembly of nanodots. When long nanosheets and nanodots assemble with each other, the period along the α-MnO_2 (110) plane is formed gradually. However, the $d_{(110)}$ spacing of 0.69 nm (Fig. 5B) is not observed in the XRD pattern of Na100-10 (Figure 1A), likely due to the limited α-MnO_2 crystallite size.

After the suspension was heated for 14 min, large numbers of nanorods appeared, coincident with the disappearance of the δ-MnO_2 nanodots (Figure 6A). The diameters of individual nanorods in Figure 6A range from 8 to 10 nm. Three nanorods attached to each other is observed in Figure 6B. Their serrated sides (Figure 5C, 6B) are smoothed (Figure 6C), most likely by dissolution-recrystallization. Meanwhile, the typical side-

to-side assembling between two nanorods is also observed in Figure 6C. There are two nanorods in Figure 6C that assembled at one end to form a continuous lattice along (110) plane. The amount of lattice dislocations observed at the attached interface (Figure 6C inset I) is more than for a single nanorod (Figure 6C inset II). The blue square in Figure 6C indicates that two nanorods separate to form a gap at one end. The (100) surface is more stable than (110) surface in solution. Therefore, two nanorods approach each other through van der Waals forces and attach themselves via the common (110) surfaces. This process has been widely reported for the growth of nanostructures by OA mechanism.[2, 42-43]

After the final heating stage, the widths and lengths of nanorods increased to ~20-40 nm and ~200-400 nm, respectively (Figure 7A, B). The serrated sides and internal lattice dislocations of nanorods in Figure 7C had almost disappeared due to the dissolution-recrystallization. However, the end of nanorods appeared scaly, caused by multiple long nanosheets and primary nanorods stacking (Figure 7C).

The coupled morphological and structural evolution. Based on the above analyses, the coupled evolutions of structure and morphology during the formation of α-MnO_2 can be illustrated in (Figure 8). Firstly, MnO_4^- is reduced by Mn(II) to produce primary nanodots of δ-MnO_2 with poor crystallinity (with crystallite size of approximately 2 to 4 nm). With increasing heating time, nanodots aggregate serially to form long nanosheets. This process is followed by the edge-to-edge OA mechanism, by which the nanodots rotate gradually to achieve the same direction within the a-b plane. Secondly, the long nanosheets stack with each other to form primary nanorods, which initiates the conversion of δ-MnO_2 into α-MnO_2. The stacking is not initially coincident because of the different sizes of long nanosheets (Figure S5, 5C, D and 7C). Finally, the primary nanorods assemble along the (110) and (001) planes by side-to-side and end-to-end OA, respectively.

Although the δ-MnO_2 did not convert to α-MnO_2 before heating for 10 min, the δ-MnO_2 nanodots attached with each other along their edges to form long nanosheets by a dynamic network of hydrogen bonds between unsaturated oxygen either from oxygen (-O), hydroxyl (-OH), or aquo-groups ($-OH_2$) at the edges of [MnO_6] octahedral layers.

This edge-to-edge OA of δ-MnO_2 was reported in a previous study.[4, 7] In this assembly process, the lower pH of 0.86 is favorable for edge-to-edge OA along the (100) plane.[7]

The structure of δ-MnO_2 produced in the initial crystallization stage does not meet the necessary conditions (high proportion of Mn(III)/Mn(II) above/below layer vacancies) for conversion to α-MnO_2 . Subsequently, the structure adjustment occurs through the production and migration of Mn(III) in the δ-MnO_2 nanodots and long nanosheets. Recently, Ling et al. showed that the amount of Mn(III) impacts the structure of δ-MnO_2. And Cui et al. revealed that the reduction of Mn(III) is unfavored for the conversion from LMOs (buserite) to TMOs (3 × 3 todorokite).[31] The Mn(III) was apparently important for the structural symmetry change and phase transformation, but the specific role it plays is unclear.[44-45] The amount of Mn(IV)/(III) for the ideal transition state structure can be counted as showed in Figure S7, i.e the interlayer Mn(III) content requires to reach 30 mol % of total Mn to meet assembly into 2 × 2 α-MnO_2. This agrees very well with our experimental observation. The AOS of Na100-10 and K100-4, the production of onset of transformation into 2 × 2 α-MnO_2 is 3.70 and 3.74 (Mn(III) concentration is 30 % and 26 % of total Mn), respectively. Sufficient Mn(III) is required for the formation the 2 × 2 tunnels 'walls' to support the transformation and providing sufficient hydrogen bonding. One possibility is that the Mn(III) is produced at low pH through the oxidation of water by layer Mn(IV) and the generation of oxygen vacancies. Indeed, [Mn(III)O_6] octahedra are distorted by Jahn-Teller effect, and bonding distortion within the octahedral layer is relieved when Mn(III) migrates from layers to the above and below the resulting vacancies (Figure 8B, step 1).[11] These [Mn(III)O_6] octahedra include three unsaturated oxygen which combined with H^+ to form -OH. When the amount of -OH is large enough, a network of hydrogen bonds forms between [Mn(III)O_6] octahedra of adjacent nanosheets and nanodots (Figure 8B, step 2, 3). These [Mn(III)O_6] octahedra dehydrate via a condensation reaction and form the 2 × 2 tunnels 'walls'. Therefore, the number of -OH is expected to be maximum at the initial stage of the transformation and then to decrease during subsequent transformation stages. These long nanosheets and nanodots attach along (001) plane of δ-MnO_2 to form α-MnO_2 primary nanorods by face-to-face OA (Figure 8B, step 4).

To confirm this formation mechanism in the α-MnO_2 with different tunnel cations, the K^+-stabilized was synthesized using the similar procedures, only $NaMnO_4$ was replaced by $KMnO_4$. During the synthesis of K^+-stabilized α-MnO_2, all trends of structure evolution are consistent with that during Na^+-stabilized α-MnO_2 synthesis (Figure S4 and Table S1, S2). It is suggested that the different tunnel cations α-MnO_2 experience the similar OA formation process. The δ-MnO_2 converted to α-MnO_2 at heating 100 ℃ for 2 min (Figure S4) indicates the rate of K^+-stabilized δ-MnO_2 conversion is much faster than that of Na^+-stabilized δ-MnO_2. The structure of K^+-stabilized α-MnO_2 was stable when the suspension was aged for 24 h, and previous reports.[16] indicate that stable (100) surface of nanorods can be formed during this stage. However, when the Na^+-stabilized δ-MnO_2 was continuously aged under 60 ℃ for 24 h, the XRD patterns of the samples show a new peak d_{hkl} = 0.4 nm of γ-MnO_2 with a 1 × 2 tunnel structure (Figure S2). The intensity of this peak increased during aging for 24 h. The Na^+-stabilized α-MnO_2 has only small quantities of Na^+ (3.24 ± 0.09% in Table 2) in the tunnel to stabilize the tunnel structure. The α-MnO_2 with empty tunnels is unstable. These results indicate that the K^+ adsorbed on δ-MnO_2 not only accelerated the production and migration of Mn(III) δ-MnO_2, but also promote the structural conversion to and stability of the produced α-MnO_2. This finding agrees well with previous reports that the K^+ ions play important roles in templating and stabilizing the tunneled framework.[46] Another differences between K^+-stabilized α-MnO_2 and Na^+-stabilized α-MnO_2 is the dominant side crystallographic face of the products. In this study, the cutting of the nanorods of Na^+-stabilized α-MnO_2 along the (001) plane at different stages shows that the side planes of nanorods still correspond with the (110) plane (Figure 7D). This is perhaps in part because the open tunnel structure is formed easier in the assembly process, and the morphology can be better captured during slower Na synthesis. In the presence of K^+, the side faces of the nanorods become four (100) faces with lower energy through dissolution-recrystallize).[16] Therefore, α-MnO_2 nanorods with different exposed lattice faces can be controlled in the synthesis according to specific application. The Na^+-stabilized α-MnO_2 is more suitable to produce nanorods with four (110) lateral face, which likely reduces the distance and

energy barrier for ion diffusion, improving the rate performance of α-MnO_2 in applications such as rechargeable battery electrodes,[47-48] supercapacitors and Li-O_2 battery catalysts.[14, 48-52] The K^+-stabilized α-MnO_2, on the other hand, is more suitable to produce long nanowires because of a stable tunnel structure with support of K^+ that does not collapse easily.

Although this study is not exhaustive, it does highlight an important area for further work on morphology and structure interaction. Indeed, future studies could include K^+ ion template effects on migration of Mn(III) into tunnel 'walls' and the changes in reactivities of the products which are formed in different stages.

CONCLUSION

Na^+-stabilized tunnel structured α-MnO_2 nanorods are found to assemble via the staged oriented attachment (OA) growth process. The coupling evolution of structures and morphologies during the whole process has been explored.

Firstly, the poorly-crystalline δ-MnO_2 nanodots aggregated along (110) surface to form δ-MnO_2 long nanosheets via the edge-to-edge OA mechanism. Meanwhile, the Mn(IV) in the [MnO_6] octahedral layer of δ-MnO_2 were reduced to Mn(III) by water, and then migrated to above and below the vacancies. Secondly, the morphology and structure of δ-MnO_2 evolved simultaneously. The Mn(III), whose amount increased gradually, build up tunnel walls and triggered conversion of the 2D layer structure to the 1D tunnel structure. A dynamic network of hydrogen bonds between -OH which combined with Mn(III) of adjacent long nanosheets are present as a mode of bonding to construct the tunnel structure. Therefore, adjacent long nanosheets aggregated and formed α-MnO_2 primary nanorods by a face-to-face OA mechanism. Thirdly, primary nanorods assemble with each other to form longer and wider nanorods by end-to-end and side-to-side OA mechanism, respectively. The defects which formed by assembly are constantly smoothed via OR process throughout the whole reaction process. This work fills the blank in the initial stage of 1D tunnel structured α-MnO_2 formation. Meanwhile, it provides greater fundamental understanding of the relationship between the coupled structure and morphology transformation during crystal growth.

Material and Methods

Synthesis of different types of cations of cryptomelane. In a typical experiment, 8.45 g $MnSO_4 \cdot H_2O$ (0.5 M) in 100 mL of acetic acid (2 M) and 80 mL aqueous solution of $AMnO_4$ (0.4375 M, A= K or Na) were mixed together under vigorous stirring at 60 ℃. This suspension was heated to 100 ℃ for 20 min and was then cool to 80 ℃. After cooling to 80 ℃, the suspension was frozen by liquid nitrogen and washed until the conductivity of the supernatant was less than 20.0 μS cm^{-1}, the suspension was then freeze-dried.

After the two solutions were mixed and the suspension was heated to 100 ℃, 10 mL of the suspension was extracted into a 50 mL centrifuge tube filled with 20 mL of liquid nitrogen at 0, 2, 4, 6, 8, 10, 14, 16 and 20 min. The extracted samples were centrifuged at 12,000 rpm for 8 min and the precipitates were washed with 50 mL of DDW multiple times until the conductivity of the supernatant was less than 20.0 μS cm^{-1}.The precipitates were then freeze-dried for characterization. Samples were labelled AMix, A100-X and A80, where X is the heating time at 100 ℃ and A is the type of cation.

Powder X-ray diffraction. The XRD patterns were collected from the dried powders using a cavity mount on a Bruker D8 Advance diffractometer equipped with a LynxEye detector, using Ni-filtered Cu Kα radiation (λ = 0.15418 nm). The diffractometer was operated at a tube voltage of 40 kV and a current of 40 mA, with a scanning rate of 1°/min and a step size of 0.02°.

Elemental analysis and Mn AOS. The chemical composition of the samples was determined by dissolving ~ 0.1 g of each powder sample in 25 mL of 0.25 mol/L $NH_2OH \cdot HCl$. The concentrations of dissolved Mn and K were measured using inductively coupled plasma (ICP) and flame spectrometry, respectively. Mn average oxidation state (AOS) was measured by a back-titration method using a $KMnO_4$ standard solution.[53]

X-ray photoelectron spectroscopy. X-ray photoelectron spectra were collected using a VG Multilab2000 X-ray photoelectron spectrometer with an Al K X-ray source

(1486 eV) and a base pressure of 3×10^{-9} Torr in the analytical chamber. The scans were recorded using the large area mode. The survey scans were collected using a fixed pass energy of 100 eV and an energy step size of 1.0 eV, whereas the narrow scans have a pass energy of 25 eV and an energy step size of 0.1 eV. The charge effect was corrected by adjusting the binding energy (BE) of C (1s) to 284.62 eV. The spectra were analyzed using the Avantage software. The Shirley-type background was subtracted before deconvolution and fitting. The parameters used by Nesbitt et al for the multiple peaks of Mn (2p3/2) for spectra fitting were adopted.[54] A 20:80 ratio of the Lorentzian: Gaussian mix-sum function was used for all the fittings.

Transmission electron microscopy. The particle size and morphology of the samples were further examined on a JEM-2100F transmission electron microscope operated at an acceleration voltage of 200 kV. Prior to observation, samples were embedded in epoxy resin, left to polymerize for 48 h in the dark and cut with an ultramicrotome (Leica EM UC6) equipped with a diamond knife. The ~50nm thick sections were picked up on lacey carbon films loaded on Cu grids. In addition to assess possible preparation-induced artefacts (use of an ultramicrotome), all sample were prepared according to the above described protocol, filtered and re-suspended in ethanol. A drop of the obtained suspension was deposited on a copper microscope grid covered with perforated carbon.

Field-emission scanning electron microscopy. Detailed three-dimensional morphologies of particles were observed by using a field emission scanning electron microscope (SU8010, Hitachi) with a maximum resolution of 1 nm. For high-resolution SEM, the microscope was operated at 15 kV and the working distance was 0.5-30 mm; an in-lens secondary electron detector was used. Prior to SEM analysis, each sample was gold-coated.

High-energy X-ray total scattering. Synchrotron-based X-ray total scattering data were collected using an X-ray energy of 58.6491 keV (λ = 0.2114 Å) at beamline 11-ID-B of the Advanced Photon Source (APS), Argonne National Laboratory (APS). The measurement was performed using the rapid acquisition PDF method by

employing a Perkin Elmer amorphous silicon detector. The image plate was exposed for 1.2 s and the measurement was repeated 75 times for a total collection time of 90 s for each sample. The software Fit2D was used to integrate and convert the 2-D raw data to 1-D intensity versus wave vector (Q) data. The PDF, G(r), was obtained from the raw 1-D data using the program PDFgetX2.

Acknowledgements

We thank Dr. GV Lowry (AE) and the anonymous reviewers for thoughtful reviews and constructive comments. The authors thank the National Natural Science Foundation of China (Grant Nos. 41471194 & 41171197) and the Strategic Priority Research Program of the Chinese Academy of Sciences (No. XDB15020402) for financial support of this research. Use of the Advanced Photon Source, Argonne National Laboratory, supported by U.S. DOE-BES under Contract DE-AC02-06CH11357.

Reference

1. Penn, L.; Banfield, J. F., Imperfect oriented attachment: Dislocation Generation in Defect-Free Nanocrystals. *Science*. **1998,** *281*, 969-971.
2. De Yoreo, J. J.; Gilbert, P. U.; Sommerdijk, N. A.; Penn, R. L.; Whitelam, S.; Joester, D.; Zhang, H.; Rimer, J. D.; Navrotsky, A.; Banfield, J. F., Crystallization by particle attachment in synthetic, biogenic, and geologic environments. *Science.* **2015,** *349*, aaa6760.
3. Zhang, J.; Huang, F.; Lin, Z., Progress of nanocrystalline growth kinetics based on oriented attachment. *Nanoscale.* **2010,** *2*, 18-34.
4. Liang, X.; Zhao, Z.; Zhu, M.; Liu, F.; Wang, L.; Yin, H.; Qiu, G.; Cao, F.; Liu, X.; Feng, X., Self-assembly of birnessite nanoflowers by staged three-dimensional oriented attachment. *Environ. Sci.: Nano.* **2017,** *4,* 1656-1669.
5. Zhao, H.; Zhu, M.; Li, W.; Elzinga, E. J.; Villalobos, M.; Liu, F.; Zhang, J.; Feng, X.; Sparks, D. L., Redox Reactions between Mn(II) and Hexagonal Birnessite Change Its Layer Symmetry. *Environ. Sci. Technol.* **2016,** *50*, 1750-1758.

6. Qian, W.; Liao, X.; Xu, W.; Yang, R.; Livi, K. J.; Zhu, M., Synthesis of Birnessite in the Presence of Phosphate, Silicate, or Sulfate. *Inorg. Chem.* **2016,** *55*, 10248-10258.

7. Marafatto, F. F.; Lanson, B.; Peña, J., Crystal growth and aggregation in suspensions of δ-MnO_2 nanoparticles: implications for surface reactivity. *Environ. Sci.: Nano.* **2018,** *5,* 497-508.

8. Atkins, A. L.; Shaw, S.; Peacock, C. L., Nucleation and growth of todorokite from birnessite: Implications for trace-metal cycling in marine sediments. *Geochim Cosmochim Ac.* **2014,** *144*, 109-125.

9. Suib, S. L., ChemInform Abstract: Porous Manganese Oxide Octahedral Molecular Sieves and Octahedral Layered Materials. *Accounts Chem Res.* **2008,** *41*, 479-487.

10. Dharmarathna, S.; King'Ondu, C. K.; Pedrick, W.; Pahalagedara, L.; Suib, S. L., Direct Sonochemical Synthesis of Manganese Octahedral Molecular Sieve (OMS-2) Nanomaterials Using Cosolvent Systems, Their Characterization, and Catalytic Applications. *Chem Mater.* **2012,** *24* , 705–712.

11. Grangeon, S.; Fernandezmartinez, A.; Warmont, F.; Gloter, A.; Marty, N.; Poulain, A.; Lanson, B., Cryptomelane formation from nanocrystalline vernadite precursor: a high energy X-ray scattering and transmission electron microscopy perspective on reaction mechanisms. *Geochem T.* **2015,** *16*, 12.

12. Grangeon, S.; Lanson, B.; Lanson, M., Solid-state transformation of nanocrystalline phyllomanganate into tectomanganate: influence of initial layer and interlayer structure. *Acta Crystallogr B Struct Sci Cryst Eng Mater.* **2014,** *70*, 828-838.

13. Liu, J.; Makwana, V.; Cai, J.; Suib, S. L.; Aindow, M., Effects of Alkali Metal and Ammonium Cation Templates on Nanofibrous Cryptomelane-type Manganese Oxide Octahedral Molecular Sieves (OMS-2). *J. Phys. Chem. B.* **2003,** *107*, 9185-9194.

14. Truong, T. T.; Liu, Y.; Ren, Y.; Trahey, L.; Sun, Y., Morphological and crystalline evolution of nanostructured MnO_2 and its application in lithium-air batteries. *Acs Nano.* **2012,** *6* , 8067-8077.

15. Li, K.; Chen, J.; Peng, Y.; Lin, W.; Yan, T.; Li, J., The relationship between surface open cells of α-MnO_2 and CO oxidation ability from a surface point of view. *J. Mater. Chem. A.* **2017,** *5,* 20911-20921.

16. Yuan, Y.; Nie, A.; Odegard, G. M.; Xu, R.; Zhou, D.; Santhanagopalan, S.; He, K.; Asayeshardakani, H.; Meng, D. D.; Klie, R. F., Asynchronous Crystal Cell Expansion during Lithiation of K^+-Stabilized α-MnO_2. *Nano Lett.* **2015,** *15*, 2998–3007.

17. Grangeon, S.; Lanson, B.; Lanson, M., Solid-state transformation of nanocrystalline phyllomanganate into tectomanganate: influence of initial layer and interlayer structure. *Acta Crystallogr. B.* **2014,** *70* , 828–838.

18. Portehault, D.; Cassaignon, S.; Baudrin, E.; Jolivet, J. P., Structural and morphological control of manganese oxide nanoparticles upon soft aqueous precipitation through MnO_4^-/Mn^{2+} reaction. *J. Mater. Chem.* **2009,** *19*, 2407-2416.

19. Portehault, D.; Cassaignon, S.; Baudrin, E.; Jolivet, J., Morphology Control of Cryptomelane Type MnO_2 Nanowires by Soft Chemistry. Growth Mechanisms in Aqueous Medium. *Chem Mater.* **2007,** *19*, 5410-5417.

20. Mckenzie, R. M., The Synthesis of Birnessite, Cryptomelane, and Some Other

Oxides and Hydroxides of Manganese. *Mineral Mag.* **1971,** *38*, 493-502.
21. Villalobos, M.; Toner, B.; Bargar, J.; Sposito, G., Characterization of the manganese oxide produced by pseudomonas putida strain MnB1. *Geochim. Cosmochim. Ac.* **2003,** *67*, 2649-2662.
22. Drits, V. A.; Lanson, B.; Gaillot, A. C., Birnessite polytype systematics and identi cation by powder X-ray diffraction. *Am Mineral.* **2007,** *92*, 771-788.
23. Grangeon, S.; Lanson, B.; Miyata, N.; Tani, Y.; Manceau, A., Structure of nanocrystalline phyllomanganates produced by freshwater fungi. *Am Mineral.* **2010,** *95*, 1608-1616.
24. Yin, H.; Tan, W.; Zheng, L.; Cui, H.; Qiu, G.; Liu, F.; Feng, X., Characterization of Ni-rich hexagonal birnessite and its geochemical effects on aqueous Pb 2+ /Zn 2+ and As(III). *Geochim. Cosmochim. Ac.* **2012,** *93* , 47-62.
25. Portehault, D.; Cassaignon, S.; Nassif, N.; Baudrin, E.; Jolivet, J. P., A core-corona hierarchical manganese oxide and its formation by an aqueous soft chemistry mechanism. *Angew. Chem. Int. Edit.* **2008,** *120*, 6541-6544.
26. Luo, J.; Zhang, Q.; Suib, S., Mechanistic and Kinetic Studies of Crystallization of Birnessite. *Inorg. Chem.* **2000,** *39*, 741-747.
27. Manceau, A.; Marcus, M. A.; Grangeon, S.; Lanson, M.; Lanson, B.; Gaillot, A. C.; Skanthakumar, S.; Soderholm, L., Short-range and long-range order of phyllomanganate nanoparticles determined using high-energy X-ray scattering. *J. Appl. Crystallogr.* **2013,** *46*, 193–209.
28. Petkov, V.; Ren, Y.; Saratovsky, I.; Pastén, P.; Gurr, S. J.; Hayward, M. A.; Poeppelmeier, K. R.; Gaillard, J. F., Atomic-Scale Structure of Biogenic Materials by Total X-ray Diffraction: A Study of Bacterial and Fungal MnOx. *Acs Nano.* **2009,** *3* (2), 441-5.
29. Zaharieva, I.; Chernev, P.; Risch, M.; Klingan, K.; Kohlhoff, M.; Fischer, A.; Dau, H., Electrosynthesis, functional, and structural characterization of a water-oxidizing manganese oxide. *Energ. Environ. Sci.* **2012,** *5*, 7081-7089.
30. Yin, H.; Liu, F.; Feng, X.; Hu, T.; Zheng, L.; Qiu, G.; Koopal, L. K.; Tan, W., Effects of Fe doping on the structures and properties of hexagonal birnessites – Comparison with Co and Ni doping. *Geochim. Cosmochim. Ac.* **2013,** *117* , 1-15.
31. Yin, H.; Feng, X.; Qiu, G.; Tan, W.; Liu, F., Characterization of Co-doped birnessites and application for removal of lead and arsenite. *J. Hazard. Mater.* **2011,** *188*, 341-349.
32. Cui, H.; Liu, X.; Tan, W.; Feng, X.; Liu, F.; Daniel Ruan, H., Influence of Mn(III) Availability on the Phase Transformation From Layered Buserite to Tunnel-structured Todorokite. *Clays. Clay. Miner.* **2008,** *56* , 397-403.
33. Stone, A. T., Reductive Dissolution of Manganese(III/Iv) Oxides by Substituted Phenols. *Environ. Sci. Technol.* **1987,** *2*, 979-988.
34. Hou, J.; Li, Y.; Liu, L.; Ren, L.; Zhao, X., Effect of giant oxygen vacancy defects on the catalytic oxidation of OMS-2 nanorods. *J. Mater. Chem. A.* **2013,** *1*, 6736-6741.
35. Xing, M.; Zhang, J.; Chen, F.; Tian, B., An economic method to prepare vacuum activated photocatalysts with high photo-activities and photosensitivities. *Chem Commun (Camb).* **2011,** *47*, 4947-4949.

36. Wang, K.; Chang, Y.; Lv, L.; Long, Y., Effect of annealing temperature on oxygen vacancy concentrations of nanocrystalline CeO_2 film. *Appl. Surf. Sci.* **2015,** *351*, 164-168.
37. Sun, Y.; Yan, X.; Zheng, X.; Liu, Y.; Shen, Y.; Zhang, Y., Influence of carrier concentration on the resistive switching characteristics of a ZnO-based memristor. *Nano Res.* **2016,** *9*, 1116-1124.
38. Holgado, J. P.; Munuera, G.; Espinós, J. P.; González-Elipe, A. R., XPS study of oxidation processes of CeO_x defective layers. *Appl. Surf. Sci.* **2000,** *158*, 164-171.
39. Li, X.; Ma, J.; Yang, L.; He, G.; Zhang, C.; Zhang, R.; He, H., Oxygen Vacancies Induced by Transition Metal Doping in gamma-MnO_2 for Highly Efficient Ozone Decomposition. *Environ Sci Technol.* **2018,** *52,* 12685-12696.
40. Zhang, G.; Dong, W.; Huang, X.; Zou, J., Oxygen vacancy induced enhancement of photochemical water oxidation on calcium manganese oxide catalyst. *Catal Commun.* **2017,** *89*, 117-120.
41. Dawson, J. A.; Tanaka, I., Oxygen vacancy formation and reduction properties of β-MnO_2 grain boundaries and the potential for high electrochemical performance. *Acs. Appl. Mater. Inter.* **2014,** *6*, 17776-17784.
42. Feng, X. H.; Zhai, L. M.; Tan, W. F.; Liu, F.; He, J. Z., Adsorption and redox reactions of heavy metals on synthesized Mn oxide minerals. *Environ Pollut.* **2007,** *147*, 366-373.
43. Zhang, H.; De Yoreo, J. J.; Banfield, J. F., A unified description of attachment-based crystal growth. *Acs Nano,* **2014,** *8*, 6526-6530.
44. Zhang, H.; Banfield, J. F., Interatomic Coulombic interactions as the driving force for oriented attachment. *Crystengcomm.* **2014,** *16*, 1568-1578.
45. Ling, F. T.; Post, J. E.; Heaney, P. J.; Ilton, E. S., The relationship between Mn oxidation state and structure in triclinic and hexagonal birnessites. *Chem Geol.* **2018,** *479,* 216-227.
46. Yang, P.; Lee, S.; Post, J. E.; Xu, H.; Wang, Q.; Xu, W.; Zhu, M., Trivalent manganese on vacancies triggers rapid transformation of layered to tunneled manganese oxides (TMOs): Implications for occurrence of TMOs in low-temperature environment. *Geochim. Cosmochim. Ac* **2018,** *240*, 173-190.
47. Wei, C.; Xu, C.; Li, B.; Du, H.; Nan, D.; Kang, F., Anomalous effect of K ion on crystallinity and capacitance of the manganese dioxide. *J. Power. Sources.* **2013,** *225*, 226-230.
48. Li, L.; Nan, C.; Lu, J.; Peng, Q.; Li, Y., α-MnO_2 nanotubes: high surface area and enhanced lithium battery properties. *Chem Commun.* **2012,** *48* , 6945-6947.
49. Arthur, T. S.; Zhang, R.; Chen, L.; Glans, P. A.; Fan, X.; Guo, J.; Mizuno, F., Understanding the Electrochemical Mechanism of K-αMnO_2 for Magnesium Battery Cathodes. *Acs. Appl. Mater. Inter.* **2014,** *6* , 7004-7008.
50. Hutchings, G. S.; Rosen, J.; Smiley, D.; Goward, G. R.; Bruce, P. G.; Jiao, F., Environmental In Situ X-ray Absorption Spectroscopy Evaluation of Electrode Materials for Rechargeable Lithium–Oxygen Batteries. *J. Phys. Chem. C.* **2014,** *118* , 12617-12624.
51. Qin, Y.; Lu, J.; Du, P.; Chen, Z.; Ren, Y.; Wu, T.; Miller, J. T.; Wen, J.; Miller, D.

J.; Zhang, Z., fabrication of porous-carbon-supported α-MnO nanorods at room temperature: application for rechargeable Li–O batteries. *Energ. Environ. Sci.* **2013,** *6*, 519-531.

52. Xiao, W.; Xia, H.; Fuh, J. Y. H.; Lu, L., Growth of single-crystal α-MnO_2 nanotubes prepared by a hydrothermal route and their electrochemical properties. *J. Power. Sources.* **2009,** *193*, 935-938.

53. Zhai, D.; Li, B.; Xu, C.; Du, H.; He, Y.; Wei, C.; Kang, F., A study on charge storage mechanism of α-MnO_2 by occupying tunnels with metal cations (Ba^{2+}, K^+). *J. Power. Sources.* **2011,** *196*, 7860-7867.

54. Kijima, N.; Yasuda, H.; Sato, T.; Yoshimura, Y., Preparation and Characterization of Open Tunnel Oxide α-MnO_2 Precipitated by Ozone Oxidation. *J. Solid. State Chem.* **2001,** *159*, 94-102.

55. Banerjee, D.; Nesbitt, H. W., XPS study of dissolution of birnessite by humate with constraints on reaction mechanism. *Geochim. Cosmochim. Ac.* **2001,** *65*, 1703-1714.

Table 1. Near-surface compositions of Mn and O species derived from fittings of Mn ($2p_{3/2}$) and O (1s).

Samples	Mn			O		
	Mn(III) (±0.003)	Mn(II) (±0.001)	Mn(IV) (±0.003)	O^{2-}	OH^-	H_2O
NaMix	0.143	0.022	0.835	0.699	0.181	0.120
Na100-4	0.123	0.048	0.829	0.621	0.224	0.155
Na100-10	0.153	0.042	0.805	0.562	0.263	0.175
Na100-14	0.134	0.041	0.825	0.610	0.229	0.161
Na80	0.130	0.017	0.853	0.685	0.192	0.123

Table 2. Na^+ content, average oxidation states (AOS) of Mn in intermediate products at various time intervals during Na^+-stabilized α-MnO_2 formation obtained from titration and fittings of Mn ($2p_{3/2}$)

Samples	XPS (± 0.02)	Titration	Chemical Composition
NaMix	3.81	3.96 ± 0.01	$Na_{0.029}MnO_{1.994}{\cdot}0.54H_2O$
Na100-0	-	3.96 ± 0.02	$Na_{0.039}MnO_{1.999}{\cdot}0.63H_2O$
Na100-4	3.78	3.86 ± 0.02	$Na_{0.055}MnO_{1.957}{\cdot}0.77H_2O$
Na100-6	-	3.75 ± 0.03	-

Na100-10	3.76	3.70 ± 0.01	$Na_{0.090}MnO_{1.895}\cdot 0.86H_2O$
Na100-14	3.78	3.78 ± 0.04	$Na_{0.067}MnO_{1.923}\cdot 0.57H_2O$
Na100-16	-	3.95 ±0.02	$Na_{0.061}MnO_{2.006}\cdot 0.67H_2O$
Na100-18	-	3.98 ± 0.03	$Na_{0.057}MnO_{2.018}\cdot 0.62H_2O$
Na100-20	-	3.96 ± 0.01	$Na_{0.048}MnO_{2.004}\cdot 0.53H_2O$
Na80	3.83	3.92 ± 0.02	$Na_{0.032}MnO_{1.976}\cdot 0.67H_2O$

665

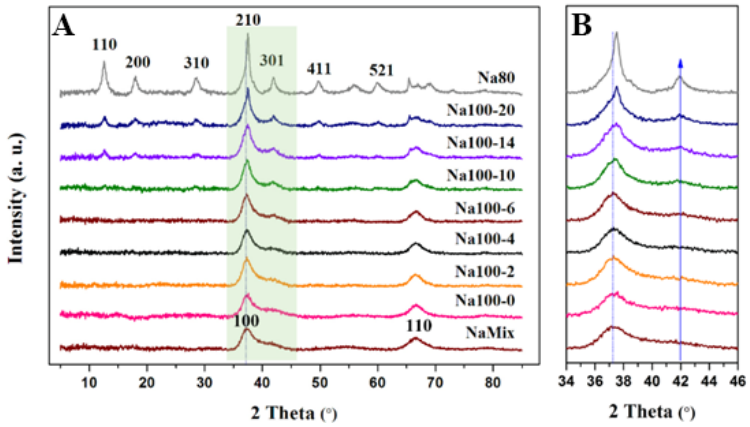

Figure 1. (A) XRD patterns of intermediate products at different intervals of Na^+ stabilized α-MnO_2 formation and crystal growth; (B) The green zone is shown magnified on the right..

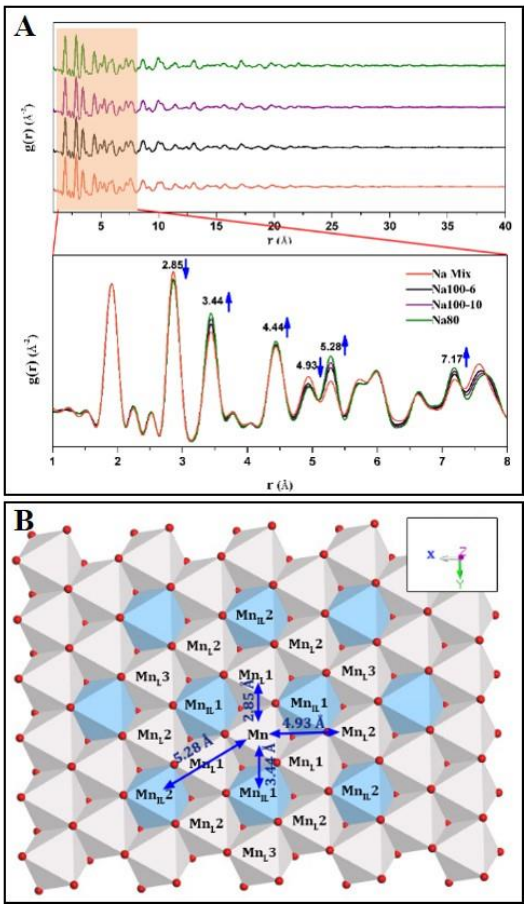

Figure 2. (A) Pair distribution functions [G(r)] of intermediate products at different intervals of Na^+ stabilized α-MnO_2 formation and crystal growth; (B) Scheme of a δ-MnO_2 layer which containing 1/3 vacancy (blue octahedral) per layer octahedron, seen along *c*-axis. The Mn_LX (X = 1, 2 or 3) means the first, second and third Mn shells around a given Mn. The $Mn_{IL}Y$ (Y= 1 or 2) means pairs formed by layer Mn and Mn at vacancies belonging respectively to the first and second shells.

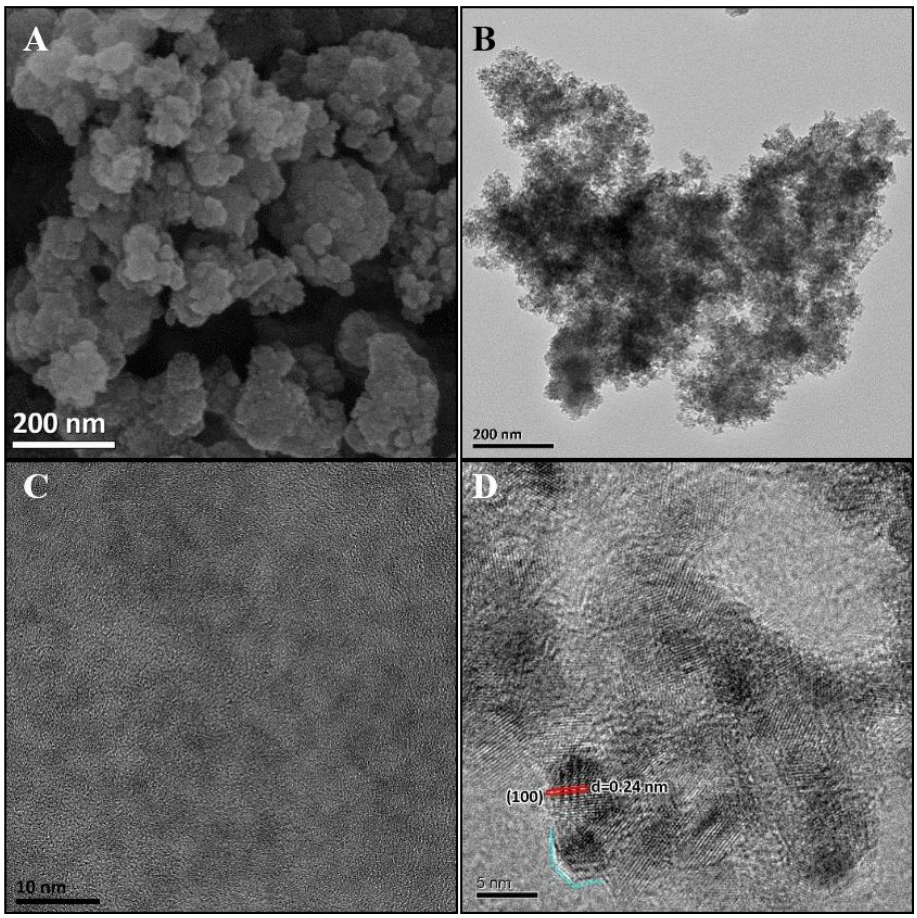

Figure 3. FESEM image of intermediate product of NaMix (A), TEM image (B and C) and HRTEM image (D) showing δ-MnO_2 nanoparticles. The blue contour of the particles (D) indicates that it is hexagonal in shape.

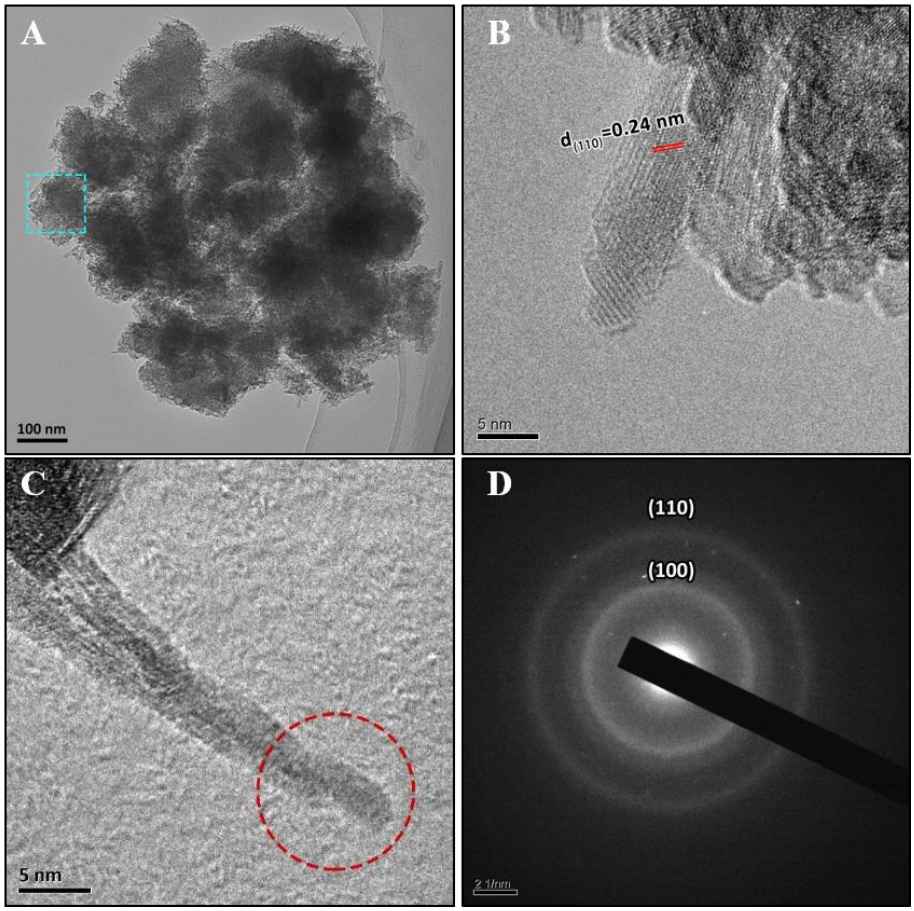

Figure 4. TEM (A) image of Na100-6. (B) shows the jagged edges of the nanosheets. (C) particle assemble on the end of nanosheets. The red circle in image C highlights the dislocation caused by primary nanodots assembly. (D) The SAED pattern recorded by focusing the electron beam in the area highlighted by the blue square in image A.

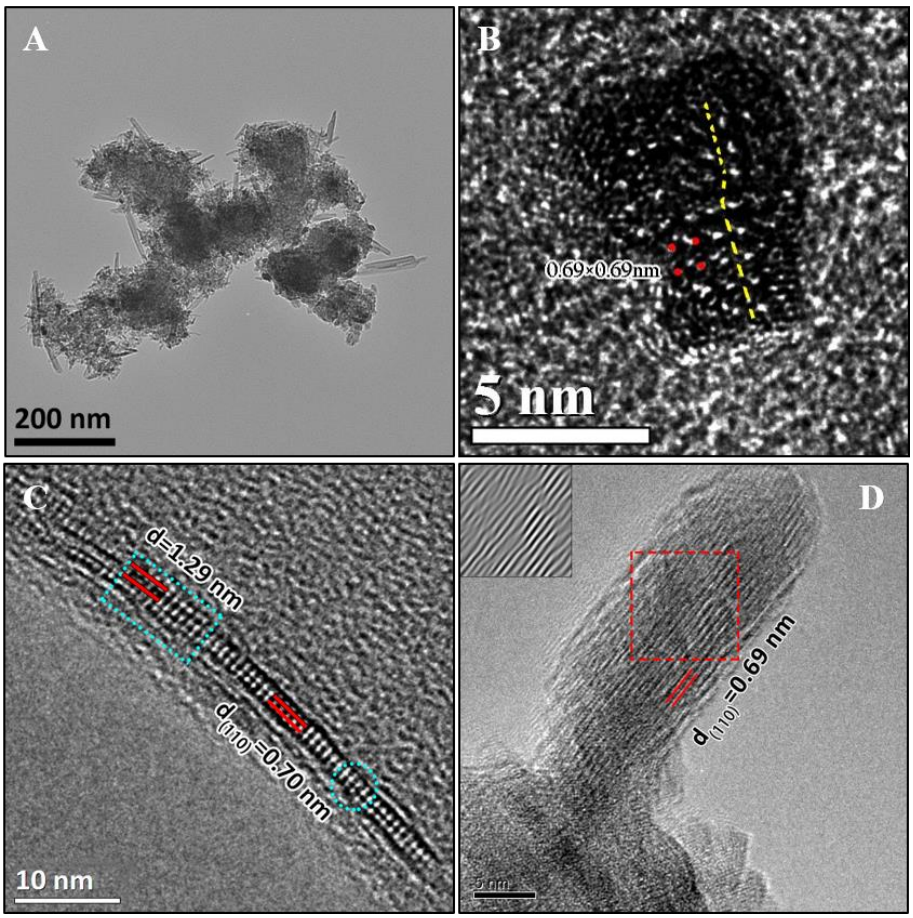

Figure 5. TEM (A) images of the intermediate Na100-10. (B)HRTEM image of an α-MnO_2 primary nanorod cross section viewed along the [001] zone axis. (C) HRTEM image of the δ-MnO_2 long nanosheet cross section view along the [100] zone axis. The blue circle indicates nanodots assembled along the (100) plane. And the blue square indicates nanodots assembled onto the nanosheets along the (001) plane. (D) An HRTEM image of a primary nanorod. And (D) shows the dislocation along (110) plane. Fourier filtered image (D inset) using red area outlined in (D), highlighting the defects.

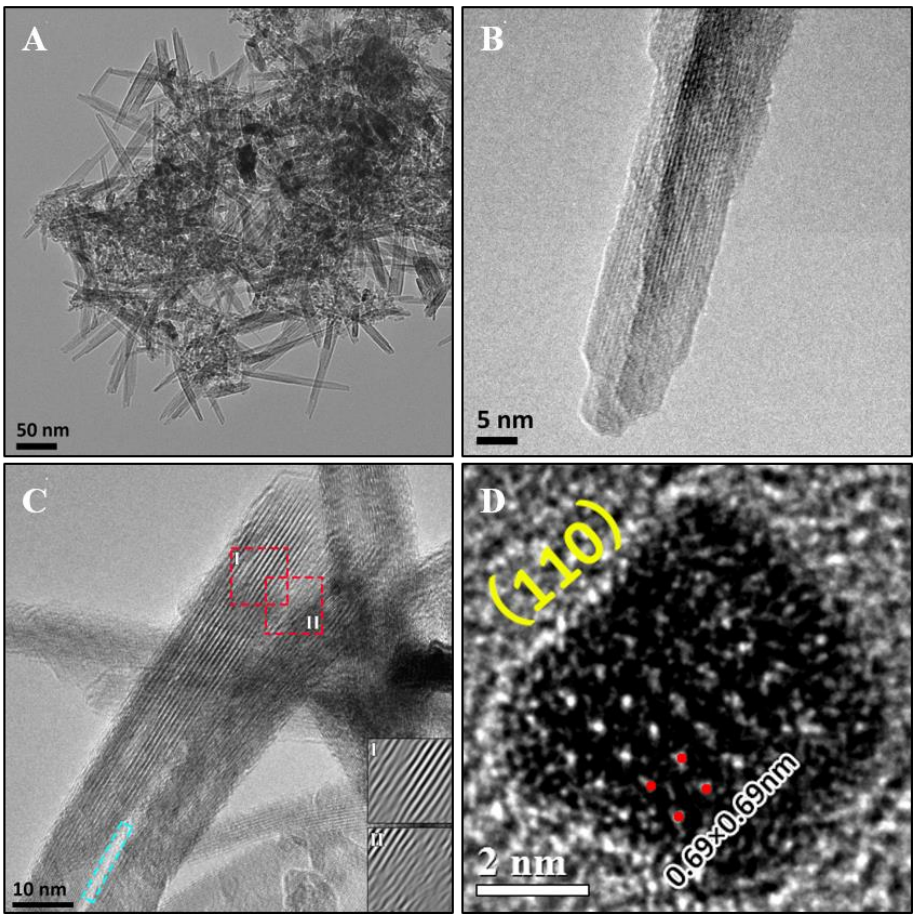

Figure 6. TEM (A) images of the intermediate Na100-14. (B, C) HRTEM images show nanorods assemble along (110) plane. The blue rectangle indicates that there is a gap between two nanorods. Fourier filtered images of zone I and zone II using red area outlined in (C), highlighting the defects. (D) An image of a nanorod cross section viewed along the [001] zone axis.

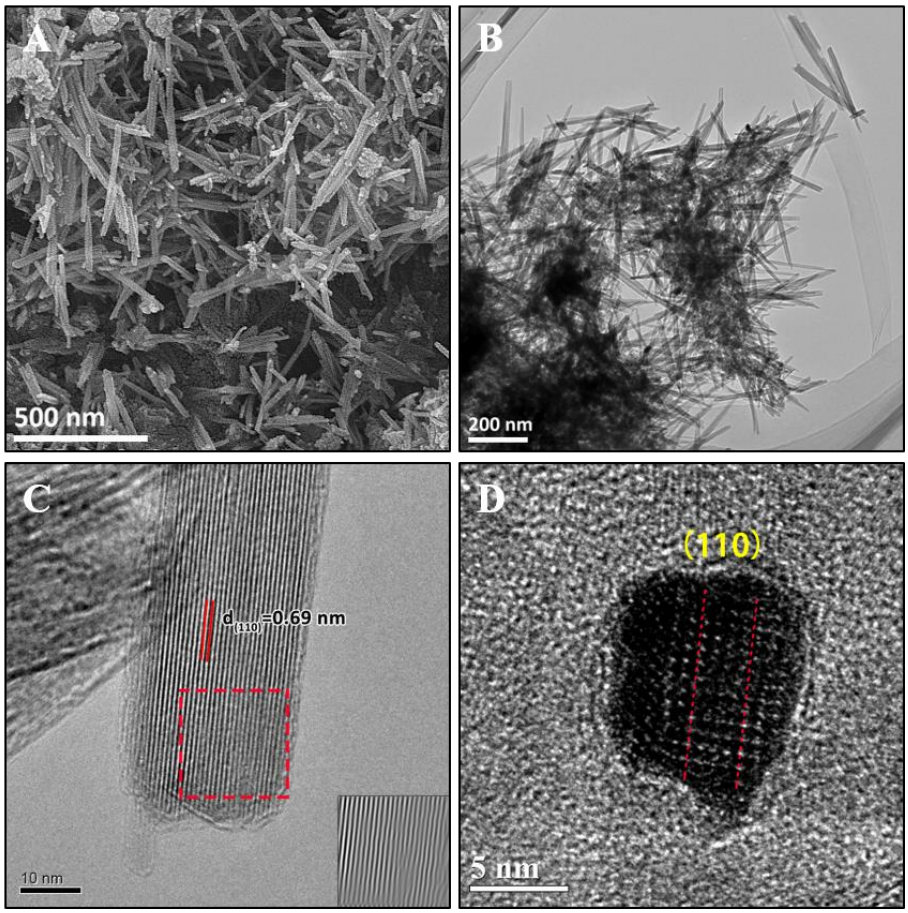

Figure 7. FESEM image of product of Na80 (A), TEM image (B) and HRTEM image (C) showing α-MnO_2 nanoparticles. Fourier filtered image (C inset) using red area outlined in (C), highlighting the defects. (D) An image of a nanorod cross section viewed along the [001] zone axis.

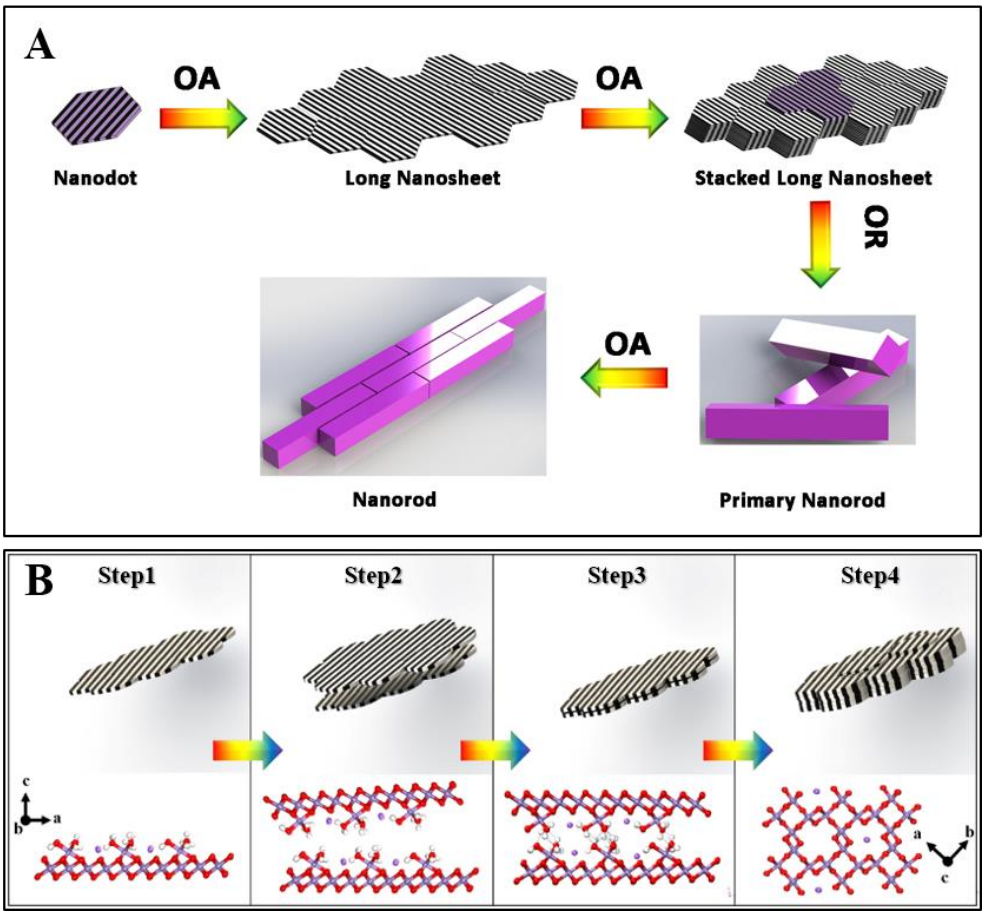

Figure 8. (A) Proposed process of assembly of nanoparticles and morphological evolution with time during crystal growth of α-MnO_2 via a staged OA process. (B) Schematic illustrating the structure changes and morphology evolutions during the δ-MnO_2 transform to α-MnO_2.